Article

Structural and Tribological Studies of "(TiC + WC)/Hardened Steel" PMMC Coating Deposited by Air Pulsed Plasma

Yuliia Chabak [1], Vasily Efremenko [1,*], Vadym Zurnadzhy [1], Viktor Puchý [2], Ivan Petryshynets [2], Bohdan Efremenko [1], Victor Fedun [1], Kazumichi Shimizu [3], Iurii Bogomol [4], Volodymyr Kulyk [5] and Dagmar Jakubéczyová [2]

1   Physics Department, Pryazovskyi State Technical University, 87555 Mariupol, Ukraine;
    chabak_y_g@pstu.edu (Y.C.); zurnadzhy_v_i@pstu.edu (V.Z.); efremenko_b_v@pstu.edu (B.E.);
    fedun_v_i@pstu.edu (V.F.)
2   Division of Metallic Systems, Institute of Materials Research, Slovak Academy of Sciences,
    04001 Kosice, Slovakia; vpuchy@saske.sk (V.P.); ipetryshynets@saske.sk (I.P.); djakubeczyova@saske.sk (D.J.)
3   Course of Robotics and Mechanical Engineering, Manufacturing and Engineering Design Center,
    Department of Engineering, Faculty of Science and Engineering, Muroran Institute of Technology,
    Muroran 050-8585, Japan; shimizu@mmm.muroran-it.ac.jp
4   Department of High-Temperature Materials and Powder Metallurgy, National Technical University of Ukraine
    "Igor Sikorsky Kyiv Polytechnic Institute", 03056 Kyiv, Ukraine; ubohomol@iff.kpi.ua
5   Department of Materials Science and Engineering, Lviv Polytechnic National University, 79013 Lviv, Ukraine;
    volodymyr.v.kulyk@lpnu.ua
*   Correspondence: efremenko_v_g@pstu.edu

Abstract: The deposition of a thin (several tens of microns) protective coating in atmospheric conditions is a challenging task for surface engineering. The structural features and tribological properties of a particle-reinforced metal matrix composite coating synthesized on middle-carbon steel by air pulse-plasma treatments were studied in the present work. The 24–31 μm thick coating of "24 vol.% (TiC + WC)/Hardened steel matrix" was produced by 10 plasma pulses generated by an electro-thermal axial plasma accelerator equipped with a consumable cathode of novel design (low-carbon steel tube filled with "TiC/WC + Epoxy resin" mixture). The study included optical microscopy (OM), scanning electron microscopy (SEM), energy-dispersive X-ray spectroscopy (EDX), X-ray diffraction (XRD, microhardness measurements, and dry "Ball-on-Plate" testing. The carbides were directly plasma-transferred to the substrate (steel of AISI 4145H grade) from the cathode without substantial melting. The hard (500–1044 HV) coating matrix consisted of 57 vol.% austenite (1.43 wt.% C) and 43 vol.% plate martensite was formed via carbon enrichment of steel from plasma flow. Additionally, a minor amount of oxide phases (TiO_2, WO_2, WO_3) were dispersed in the matrix. As compared to substrate, the coating had a lower coefficient of friction; its volumetric wear was decreased by 4.4 times when sliding against hardened steel ball and by 16 times when sliding against SiC ball.

Keywords: pulsed-plasma deposition; PMMC coating; carbide; matrix; wear resistance

1. Introduction

The composites are specific materials for different engineering applications which are consisted of dissimilar materials with different physical and mechanical properties. Due to their increased strength, the metal matrix composites are frequently used in automotive and aviation industries, cutting tools manufacturing, electronics, etc. [1]. Particle reinforced metal matrix composites (PMMCs) present the ceramic particles spread in metallic (Al-based, Ti-based, Fe-based etc.) matrix [2–4]. PMMCs are among the first options for using against erosion and wear [5] due to the synergetic interaction of hard wear-resistant particulates and a tough matrix that tightly holds the particles in a conglomerate [6,7]. Liquid metallurgy and powder consolidation are common methods for PMMCs' fabrication; however, different deposition technologies are also employed to form PMMC as a protecting coating

on a surface [8]. Electrodeposition [9], cold spraying with plasma gas atomization [10–12], resistance seam welding [13], spark plasma sintering [14], direct constrained sintering on a surface [15,16], self-propagating high-temperature synthesis [17], high-velocity oxygen fuel deposition [18], and severe plastic deformation with simultaneous addition of the reinforcing alumina powder and the air-oxidation treatment [19] were successfully used for the deposition of PMMC coatings with improved tribological properties.

Highly-concentrated energy sources (laser beam, ion beam, or plasma flow) are frequently reported as effective approaches for PMMC coating synthesis [20–22]. Kotarska et al. used laser cladding [23] to produce an Inconel/(10–40 vol.% TiC) composite with improved resistance to solid particle erosion. Li et al. [24] described the significant increase in the wear/corrosion resistance of Ni-Al-bronze due to laser surface cladding of a Co-based alloy composite reinforced by carbides (TaC, Cr_3C_2) and intermetallic (Co_3Ta) particulates with optimal properties at 20 wt.% of TaC. Tan et al. [25] attempted to in-situ synthesize Al_2O_3 ceramic and M_7C_3 carbide in the iron matrix by laser cladding to improve microhardness and dry-sliding wear properties due to complex effects of the grain refinement, precipitation hardening, and solid solution strengthening.

The plasma-related surface deposition was also applied for PMMCs coating fabrication as reported in [26–28]. Powder plasma transferred arc welding was used to consolidate a "TiC/synthetic diamond/Co-based alloy" composite featuring 140 times higher abrasive wear resistance as compared with 400 HB-heat treated steel [29]. Zhang et al. [30] applied plasma cladding for in-situ fabrication of (TiB_2 + TiC)-reinforced Ni-based alloy to decrease the friction coefficient and to prevent severe abrasive/adhesive wear under high load (up to 60 N). Rokanopoulou et al. [31] showed the effectiveness of adding TiS_2 to (Al_2O_3 + Fe) powder mixture to create a self-lubricating wear-resistant PMMC coating on duplex stainless steel 2205 surface. Huang et al. [32] utilized a plasma transferred arc process to protect Q235-carbon steel with a PMMC coating consisting of 30 wt.% Cr_3C_2 particles embedded to γ(Ni, Fe)-matrix; it was found that Cr_3C_2 carbide was partially melted to form a hyper-eutectic structure. Sivkov et al. [33] reported that a coaxial magneto-plasma accelerator generates a high-speed (~3 km·s^{-1}) plasma flow enabling the formation of a PMMC TiC/Ti coating with strong adhesion to the copper substrate due to deep penetration of titanium particles into the substrate structure. Tyurin with the colleagues applied the detonation-based pulse-plasma deposition to produce a WC/Co-Cr coating on corrosion-resistant steel [34] and a ZrB_2–$MoSi_2$ coating on a carbon/carbon conglomerates [35]. A low-temperature pulsed-plasma sintering was used in [36] to fabricate WC/Cu composites.

Among PMMC coatings, Fe-based compositions stand out for their low cost, good manufacturability, and high abrasive wear resistance [37,38]. They are mostly obtained using a mixture of Fe powder with strengthening particulates or precursors. According to Salloom et al. [39], a laser cladding of a (B_4C + 4 wt.% Fe) precursor resulted in a nano-composite with a multi-phase structure comprising B_4C, Fe_2B, and Fe_3C phases precipitated from liquid under laser melting. Iron-based (VC, TiC, WC)-containing coating was produced by diode laser to achieve improved abrasive water-jet erosion resistance [40]. PMMC coatings with an alloyed steel matrix exhibit an improved tribological behaviour due to increased matrix microhardness: hard (martensitic) matrix successfully withstands the abrasion thus preventing an easy spalling of reinforcing particles. According to this approach, Chen et al. [41] produced a H13 steel/TiC laser cladded composite with an austenite-martensite matrix and integrated microhardness of 1365 HV. A similar H13/TiC composite of increased erosion resistance was fabricated by Jiang and Kovacevic [42] via laser deposition. Gordo et al. [43] used a powder metallurgy technique to produce the NbC/TaC-reinforced PMMC with a matrix of M3/2 high-speed steel which effectively withstands wear under conditions of sliding against an alumina pin. Concluding, the alloyed steel matrix broadens the functionality of the PCCM coatings through the enhancement of the matrix properties.

Steel-based PMMC coatings can be fabricated by pulsed-plasma deposition (PPD) using an electro-thermal axial plasma accelerator (EAPA), described in [44–46]. This

installation enables the generation of high-energy plasma pulses just in the air under atmospheric pressure. An EAPA is equipped with a consumable electrode (cathode) which intensively erodes under high-current discharge inside the EAPA's internal chamber. The eroded material (as ions, atoms, or micro-droplets) is transferred by plasma flux to form a coating on the substrate surface. The EAPA cathodes made of high-Cr cast iron and high-W speed steel were previously used to synthesize the carbide/matrix composite coatings [46,47]. Since these cathode materials contained eutectic carbides (M_7C_3 or Me_6C, respectively) their plasma transfer was expected to form a PMMC coating on the substrate surface. However, as-deposited coatings had a soft austenitic microstructure without carbide reinforcement since all eutectic carbides were completely melted under high-current discharge. Owing to fast solidification, the alloying elements (Cr, Mn, W, and V) were trapped in the matrix, resulting in its stabilization. In order to stimulate in-situ carbide precipitation (with further austenite $\rightarrow$ martensite transformation) the destabilizing post-heat treatment was performed at 950 °C, leading to the "Carbide/Martensite" composite structure [46,47]. However, the high-temperature post-heat treatment may deteriorate the bulk structure/properties; therefore, the PPD technique should provide direct PMMC coating formation without additional heat treatment. This requirement can be met by using a composite electrode comprised of the hard-to-melt particulates and an easy-to-melt binder. An easy-melting binder allows for the adjustment of EAPA parameters in order to decrease the energy released under arc discharge. This could prevent carbides melting enabling their plasma transfer in a non-molten state. Such PPD-EAPA approach was previously utilized in [48] to fabricate a pulsed-plasma composite "WC/Al-bronze" coating with improved dry-sliding properties. However, it has not yet been attempted to synthesize a pulsed-plasma wear-resistant PMMC with a matrix of hardened (martensitic) steel. This task was resolved in the present work by developing a novel design of a consumable EAPA cathode.

2. Materials and Methods

2.1. EAPA Cathode Design and PPD Parameters

Pulsed plasma deposition was performed in this work using an electro-thermal axial plasma accelerator. EAPA configuration and working principles are described in detail in [44,45,49]. The EAPA consists of a 430 mm long paper-reinforced bakelite tube (8 mm inner channel diameter, 17 mm wall thickness) connected with an electrical circuit (Figure 1). The tube has steel shells (1) and (7), and the latter is used as an anode. The steel rod (2) is positioned coaxially serving as a cathode (the distance between the cathode's tip and the EAPA edge (8) is 50–70 mm). The EAPA's electric installation consists of an impulse current generator (ICG) (capacitive energy storage and a nonlinear inductance) and an impulse voltage generator (IVG) (a capacitive energy storage device of 1.5 mF, a pulse transformer, a triggered spark gap, and a decoupling capacitor). A high current (up to 18 kA) and high voltage (up to 4.5 kV) short-living (0.5–1.0 ms) arc discharge is switched on inside the EAPA's inner channel between the consumable part of the cathode and the steel shell (7) (anode). A sheet-copper cylinder (5) is intended to promote the sliding discharge inside the tube. Under the arc discharge, the inner channel walls and the electrodes' surfaces evaporate, generating plasma inside the EAPA channel. The very fast pressure increase is followed by ejecting a plasma flow out of the EAPA tube [48].The EAPA works under atmospheric pressure with air as the working gas. The time interval for charging the capacitor is 10–15 s.

The EAPA cathode has a multi-part design consisting of a consumable ending part (6) (intended for the coating deposition) and a permanent steel rod connected with an electrical circuit. The consumable part is attached to the steel rod by a copper tube mount (4). EAPA-PPD technique implies the selection of the composition of consumable part, since the coating formation proceeds through the transfer of the cathode material eroding under arc discharge inside the EAPA. Previously [46,47,50], the consumable part was a rod-shaped bulk metallic material. Alternatively, a composite structure of the cathode ending part was proposed in [48] to consist of the refractory ceramics particles and a low-melting metallic

binder. The lower melting point of a binder enables the coating deposition under low discharge voltage (meaning lower energy released inside the EAPA), ensuring that the particles will remain non-molten during plasma-transferring to the substrate surface. In this case, post-heat treatment to precipitate the carbides from a supersaturated solution is not required. When pursuing the formation of wear-resistant PMMC coatings, it is necessary to focus on directly obtaining (without heat treatment) a hard metal matrix of a plate martensite characteristic for quenched high-carbon steel [51]. In addition, the EAPA cathode should have a high electrical conductivity to ensure the arc switching between an anode and the tip of a cathode ending part. This allows an intensive erosion of the latter to form a coating of the desired composition. In the case of low electrical conductivity, the arc cathode spot moves from the consumable tip to more electrically conductive cathode parts, in particular, to the copper mount, leading to rather the erosion of the latter instead of the carbide-containing cathode part.
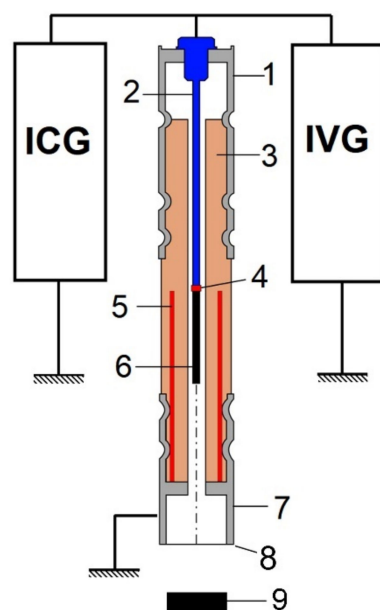

Figure 1. The principal scheme of EAPA and its electrical installation: 1, 7—steel shells, 2—cathode, 3—paper reinforced bakelite, 4—copper mount, 5—sheet copper cylinder, 6—consumable part of the cathode, 8—EAPA edge, 9—the target (the substrate) (ICG—impulse current generator, IVG—impulse voltage generator).

Based on the above considerations, a novel approach to fabricate a consumable part of the EAPA cathode was proposed in the present work. A consumable part was designed as a tube made of plain low carbon steel filled with epoxy resin-bonded ceramics particles. The steel tube as a cathode body has the following advantages: (a) high electrical conductivity of a steel tube enables a discharge between the anode and the consumable part tip, ensuring an intensive erosion of the latter; (b) the erosion of the steel tube will supply a plasma jet with iron (as atoms and micro-droplets), which is necessary to form a steel matrix of a composite; and (c) the tube can be used as a container to bear ceramics particles needed for PMMC coating formation.

The second original approach was to fill a tube by reinforcing particles bonded with epoxy resin. The use of epoxy resin instead of a metal to bind the particles has a number of advantages [52,53]: (a) an easy filler preparation (mixing instead of sintering or casting), and (b) the epoxy binder easily burns out (evaporates) under the arc discharge, releasing the ceramic particles to be directly plasma-transferred to the target.

The acquisition of a hard (plate martensite) matrix of PMMC coating presumes the following conditions: (a) the saturation of matrix with carbon, and (b) preventing the formation of an excessive amount of retained austenite (RA). The sources of carbon which can be plasma-transferred in the EAPA/PPD process are: (a) carbon of the steel tube,

(b) carbon released during the EAPA walls' erosion (evaporation), and (c) carbon released during epoxy resin burning (evaporation). The carbon saturation of the coating due to EAPA wall erosion was previously described in [46], where the volume fraction of carbide in the coating was two times as high compared to cathode material. In this regard, it is important that the tube material must be precisely low-carbon plain steel to prevent a reduce the Ms temperature due to excessive carbon saturation and/or the effect of alloying elements. Otherwise, it may lead to increased amount of retained austenite affecting coating hardness/wear resistance. The formation of martensite matrix will occur on the surface directly under PPD: mixing with iron carbon atoms forms a high-carbon liquid which solidifies to plate martensite due to ultrafast coating crystallization [54].

The burnout of the carbide/epoxy mixture ensures the release of carbide particles. The epoxy binder burns in contact with the arc (in cathode spot) and in contact with plasma moving inside the EAPA channel before ejecting. In order to increase the surface of contacting plasma flow with "carbide/epoxy" filler, it was proposed to make holes in the tube wall, thus allowing the filler come to the tube surface. In this work, the consumable cathode part was a 60 mm long steel tube of 8 mm outer diameter and 0.8 mm a wall thickness. The rows of through holes were drilled along the tube circumference with the distance between the rows of 4 mm. Each row consisted of four 2.5 mm diameter holes drilled with a step of 90°. Each subsequent row of holes was offset by 45° from the previous one, as shown in Figure 2.

Figure 2. The solid model of the consumable part of the EAPA cathode.

The tube was made of low-carbon plain steel of ASTM 1020 grade (0.15 wt.% C; 0.28 wt.% Si; 0.65 wt.% Mn; 0.010 wt.% S; 0.017 wt.% P) with "Ferrite + Pearlite" structure (Figure 3a). The mixture of WC carbide and TiC carbide powders taken in equal proportions was prepared by mixing for 4 h in a turbula type 3D-mixer (homemade, volume of 0.34 l, rotation speed is 30 min^{-1}). The carbide powder was thoroughly mixed by liquid epoxy resin in a volume ratio of 2:1. Immediately after preparation, the carbide/epoxy mixture was used to fill the tubes. After filler solidification, the consumable part of the cathode was ready for PPD. The microstructure of the indurate filler (carbides (white) + epoxy resin (dark)) is shown in Figure 3b. Carbide volume fraction was 24.9 ± 2.0 vol. %; carbide size varied in a range of 0.3–8.5 μm with the most part falling to the interval of 1–4 μm (Figure 3c). A general view of the ready consumable part of the EAPA cathode is demonstrated in Figure 3d.

The working parameters of a pulsed-plasma deposition were as follows: discharge voltage—4.0 kV; discharge duration—1 ms; distance between EAPA electrodes—50 mm; distance between EAPA edge and the target surface—50 mm; the number of pulses—10; pressure—atmospheric. The eroded surface of the cathode is depicted in Figure 3d. A target material was commercial steel of AISI 4145H grade. The specimens of 6 × 12 × 25 (mm) in size were cut from an as-rolled plate of 25 mm thick of chemical composition of 0.48 wt.% C; 0.26 wt.% Si; 0.74 wt.% Mn; 0.013 wt.% S; 0.015 wt.% P. The substrate (steel of AISI 4145H grade) had a "Ferrite + Pearlite" structure typical for middle carbon steel with a hardness of 220 HV (Figure 3e).
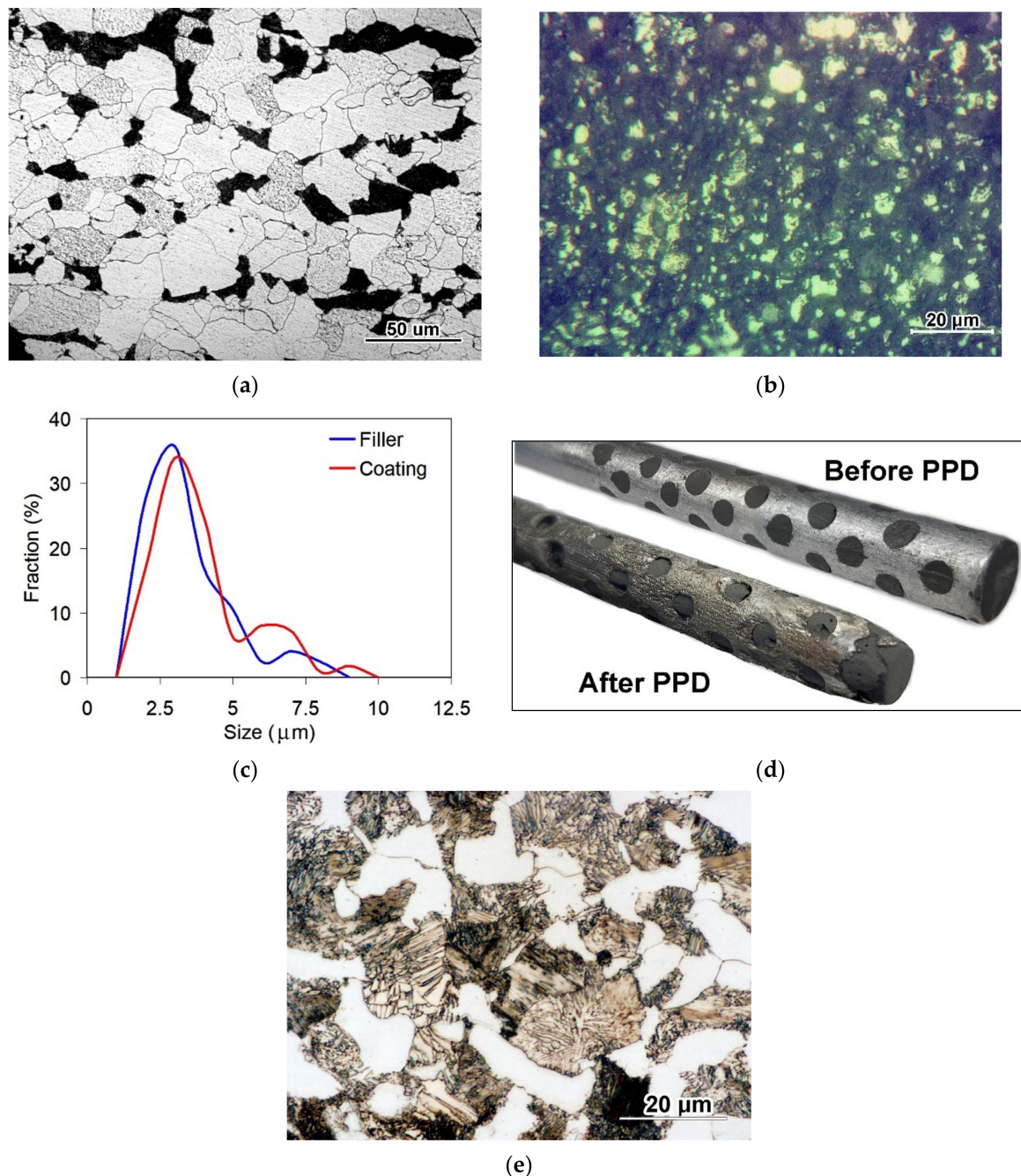
Figure 3. The consumable part of the EAPA cathode: the microstructure of (**a**) a steel tube and (**b**) a filler, (**c**) carbide size distributions for the filler and the coating, and (**d**) general view of the ready cathode before PPD (pulsed-plasma deposition) and the eroded cathode after deposition of five coatings (50 pulses). (**e**) The microstructure of a substrate (steel of AISI 4145H grade).

2.2. Coating Characterization and Dry-Sliding Testing

The coating's microstructure was studied on transversely cross-sectioned probes metallographically prepared by a multi-stage polishing for mirror state and etched by a 4 vol.% solution of nitric acid in ethanol. The microstructure was observed on the coating surface prepared according to the same procedure. The microstructural observation was performed using an optical microscope Eclipse M200 (Nikon, Tokyo, Japan) and a scanning electron microscope JSM-6510 (JEOL, Tokyo, Japan). The thickness of the coating was measured in cross-sectional SEM images along 10 lines that are 10 μm apart. The carbide size distribution was determined by manual counting of each particle using five optical

images with an area of 5500 μm^2 each. Energy-dispersive spectrometry with a detector JED-2300 (JEOL, Tokyo, Japan) was applied for phase chemical composition investigation. X-ray diffraction was employed for coating phase identification using an IV Pro (Rigaku, Tokyo, Japan) diffractometer equipped with Cu-Kα source. The volume fraction of retained austenite (f_{RA}) was calculated using the equation:

$$f_{RA} = \frac{100\%}{1 + G(I_\alpha/I_\gamma)},$$ (1)

where I_α and I_γ are the intensities of diffraction lines of αFe (200), (211) and γFe (200), (220), (311); and G is the fitting parameter for different peaks combinations [55]. The RA volume fraction was averaged for f_{RA} values calculated for different pairs of lines.

The content of carbon in retained austenite (C_{RA}) was derived from the equation:

$$a_\gamma = 0.3556 + 0.0453 \cdot C_{RA} + 0.000095 \cdot Mn,$$ (2)

where a_γ and Mn are a lattice parameter (angstrom) and manganese content (wt.%) in RA, accordingly. The lattice parameter was found as [56]:

$$a_\gamma = (h^2 + k^2 + l^2)^{0.5} \frac{\lambda}{2 \sin \theta},$$ (3)

where h, k, and l are the indices of crystallographic plane of diffraction, λ is the X-ray wave length, and θ is a Bregg angle derived from the XRD pattern.

Microhardness was measured by a FM-300 microhardness tester (Future-Tech Corp., Kawasaki, Japan) under a load of 20 g. The carbide volume fraction was calculated by the lineal Rozival method [48]. The coating's tribological behaviour was studied under the testing according to the "Ball-on-Plate" reciprocating dry-sliding scheme using a "Micron-tribo" tribometer (Micron-System, Kyiv, Ukraine). The test was performed at ambient temperature and at a relative humidity of 60–70%. Before testing, the surface of the specimen was polished to mirror state for better wear track observation (with averaged values of Ra = 0.08 μm and Ra = 0.22 μm for the substrate and the coating, accordingly). The coating served as a plate while the counter body was a 3 mm diameter ball made of hardened 100Cr6 steel AISI 52100 (63 HRC) or SiC (2600 HV). A normal load on a ball/plate contact was 5 N. The ball moved forth and back with a stroke length of 3.5 mm to make 2500 strokes and run a total sliding distance of 8.75 m. The sliding speed was 7.0 mm/s^{-1}.The recording rate was 10 readings per second, and then the data on the coefficient of friction (CoF) were averaged for each sliding cycle [57]. These cycle-averaged values were then used to calculate the mean CoF value for the entire test (without a running-in period). The dry-sliding wear resistance of the coating was assessed by the volumetric wear value derived from the wear track characterization using the profilometer "Micron-beta" (Micron-System, Kyiv, Ukraine). The volumetric wear (ΔV) value was calculated as ΔV = VL − VI, where VL is a volume loss (wear-track-deepening volume) and VI is a volume increase (wear-track-protrusions volume). VI and VL values were derived by analyzing the wear-track profile relative to the profile baseline (as shown in Figure 4). The volumetric wear of the wear track was measured in three different intervals of 785 μm length lying within the track's middle part. The same measurements were performed for three tracks obtained on each of three different specimens. The volume loss is the average value of all measurements.
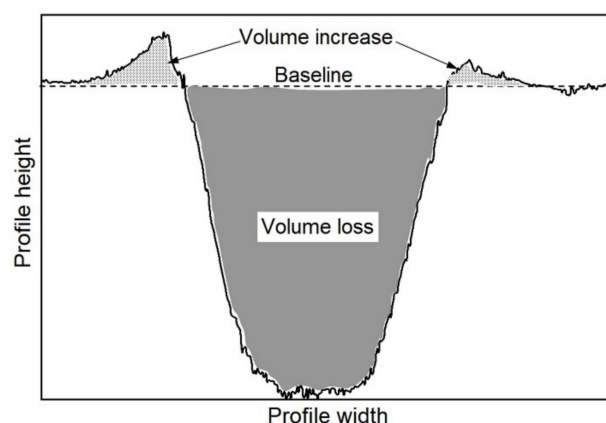
Figure 4. The scheme of the volumetric wear calculation using the wear track's profile.

3. Results

3.1. Coatings Microstructure and Phase Composition Characterization

Pulsed plasma deposition resulted in a coating of 24–31 μm thickness, shown in cross-section in Figure 5a. The coating had a typical PMMC structure consisting of compact equiaxial carbide particulates with a volume fraction of 24.1 ± 3.0 vol.% distributed within the metallic matrix (Figure 5b). The particulates were of different shapes (roundish and angular), and their size varied in a rather wide range of 0.6–12.0 μm. Most of the particles had a size of 1–3 μm; their size distribution was close to that of carbide size in the cathode filler (Figure 3c). Some particles were not tightly adjusted to the matrix: the oxide shell was seen at the carbide/matrix interface (Figure 5b). Further, the extended thick oxide films were found in the structure not to be closely associated with carbides that revealed the matrix oxidation in a plasma flow (Figure 5c). The total oxide volume fraction was estimated as 2.25 ± 0.98 vol.%. The matrix featured, in optical microscope images, a homogeneous smooth pattern, although in the carbide-free areas a needle-like pattern was revealed and attributed to plate martensite [58] (Figure 5d). Under SEM observation, some matrix areas were characterized by a thin carbide network engulfing fine matrix grains (Figure 5e).

Figure 6 depicts the results of the coating microhardness measurements. The matrix was rather hard: its microhardness varied from 500 to 1044 HV. According to the diagram (Figure 6), almost half of the measurements (41%) fell into the interval of 700–800 HV; furthermore, 67% of the values exceeded 700 HV, which corresponds to the structure of plate-martensite. The values higher than 1000 HV can be attributed to the matrix areas reinforced by a thin carbide net or fine carbide precipitation. Occasional enlarged particles were used to define carbide microhardness. It was measured as 1516–2029 HV, with most values' fractions (55%) lying in the range of 1700–2000 HV (average value of 1857 ± 151 HV) which is consistent with the data reported for tungsten carbide [59].

The phase composition of the coating was identified by X-ray diffraction. The XRD pattern of the coating (Figure 7) presents the diffraction peaks belonging to the Fe-based dual-phase (αFe + γFe) matrix as well as reinforcing carbide phases. Both αFe and γFe were characterized by intensive and multiple peaks, reflecting the predominant share of Fe-based matrix in a composite structure. According to the αFe and γFe peaks' intensities ratio, austenite slightly prevailed in the matrix with 57 vol.%. Calculation by Equations (2) and (3) gave a carbon content in austenite of 1.43 wt.%. Additionally, the multiply peaks attributed to WC and TiC carbides were identified on the XRD pattern, proving that both carbides were plasma-transferred from the cathode to the coating. Further, the weak peaks lying at $2\theta = 54$–$59°$ were uniquely associated with cementite (M_3C) carbide peaks (023) and (130). Moreover, the specific peaks at $2\theta = 38.1°$, $2\theta = 39.9°$ and $2\theta = 70.8°$ can be assigned to M_3C and W_2C both. Thus, the carbide phase composition of the coating only partly corresponded to the cathode filler carbides (WC, TiC), while M_3C and W_2C phases

were obviously newly formed during deposition. In low angles interval, some peaks are positioned that can be assigned to the oxide phases (TiO_2, WO_2, WO_3).
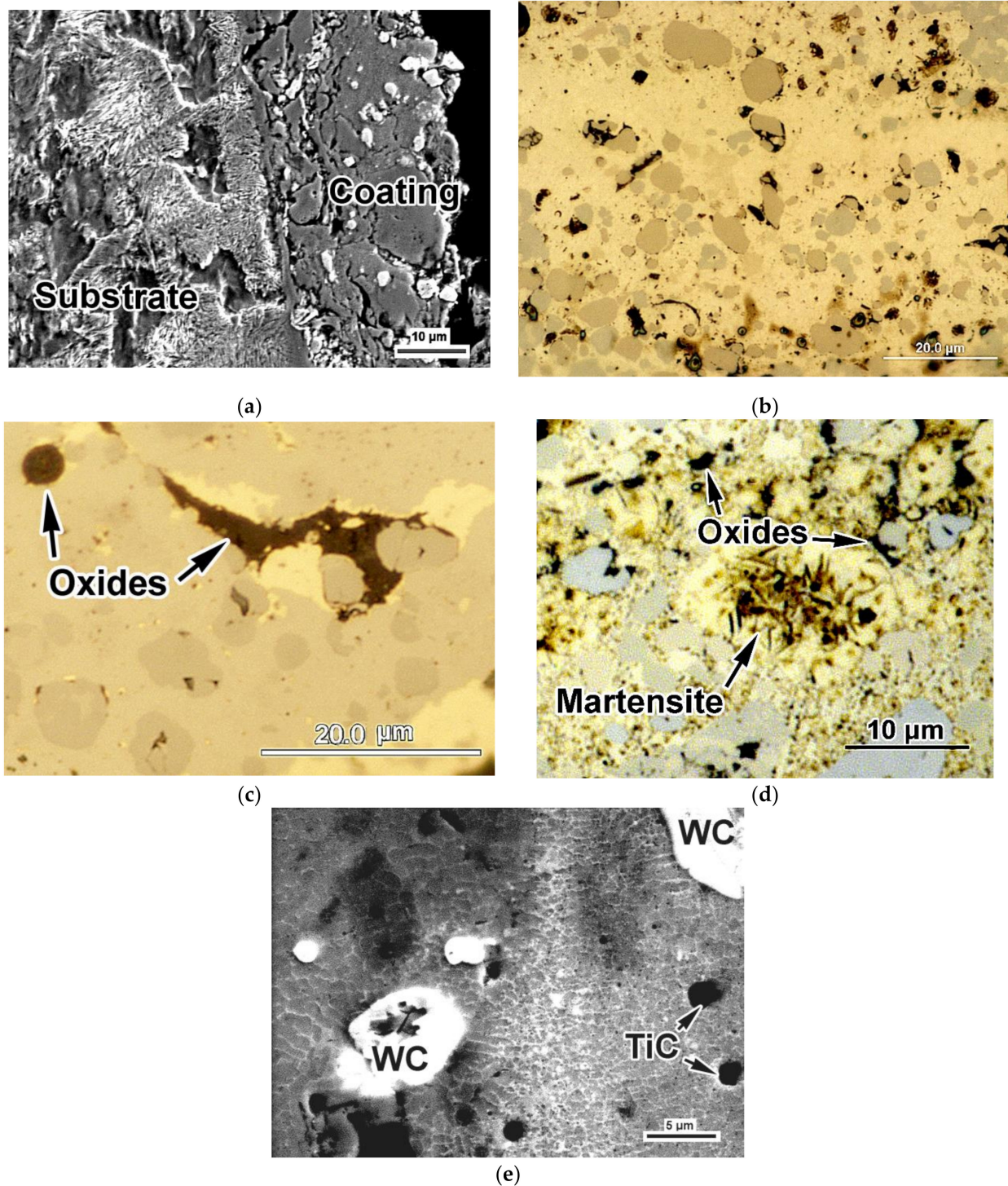

Figure 5. The coating microstructure: (**a**,**d**) cross-sectional direction, (**b**,**c**) a view from above. ((**a**)—SEM (secondary electron image—SEI); (**b**–**d**)—OM, (**e**)—SEM (back-scattered electron image—BSEI)).
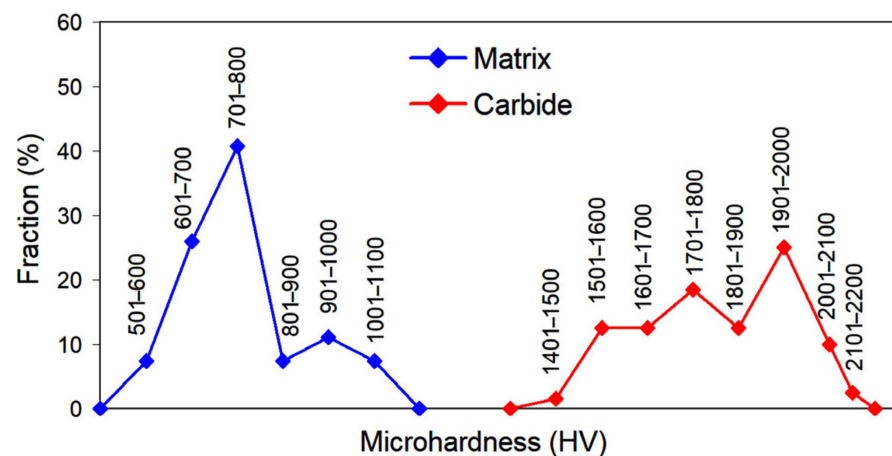
Figure 6. The coating microhardness: distribution of the values for the matrix and carbide particles.
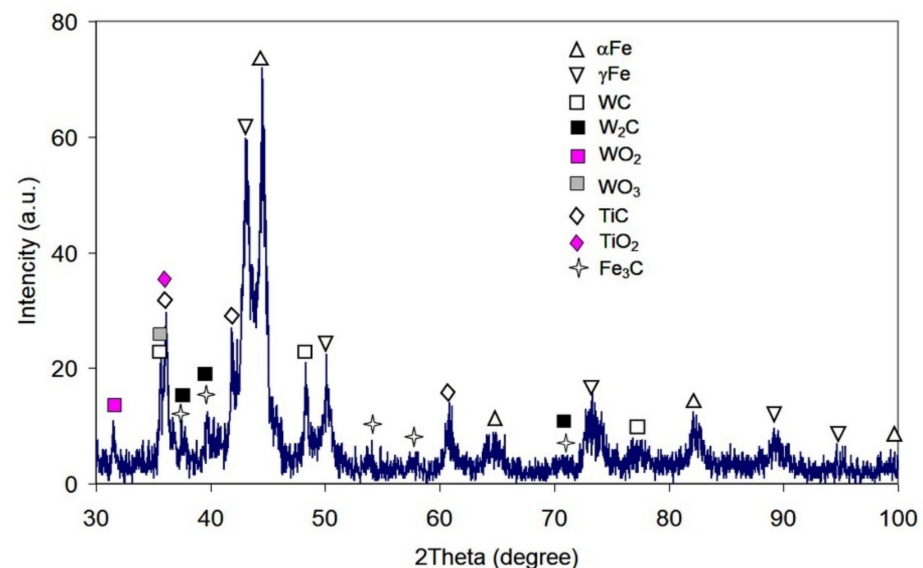

Figure 7. XRD pattern of the coating.

EDX-spectrometry was employed to assess the phase elemental distribution within the coating area shown in Figure 8a. EDX-mappings for W, Ti, Fe, and C coatings are presented in Figure 8b–e. An element concentration is qualitatively depicted on the map by a specific colour according to the colour scale (left side of the map) to vary from 0 wt.% (black colour) to 100 wt.% (white colour). Coarse TiC and WC carbides are clearly distinguished in Figure 8b,c accordingly as the white spots meaning high concentrations of tungsten/titanium. As seen, the location of white spots does not match, which indicates that titanium and tungsten were not mutually fused under their plasma transfer to the substrate. It is noteworthy that carbides were enveloped by the colourized halo revealing the partial dilution of these elements in the surrounding matrix. Iron was concentrated in a matrix with no visual trace in coarse carbides (Figure 8d). As follows from Figure 6e, the distribution of carbon was mostly associated with carbide particles. The oxygen distribution was associated with the oxide conglomerates (Figure 8f).
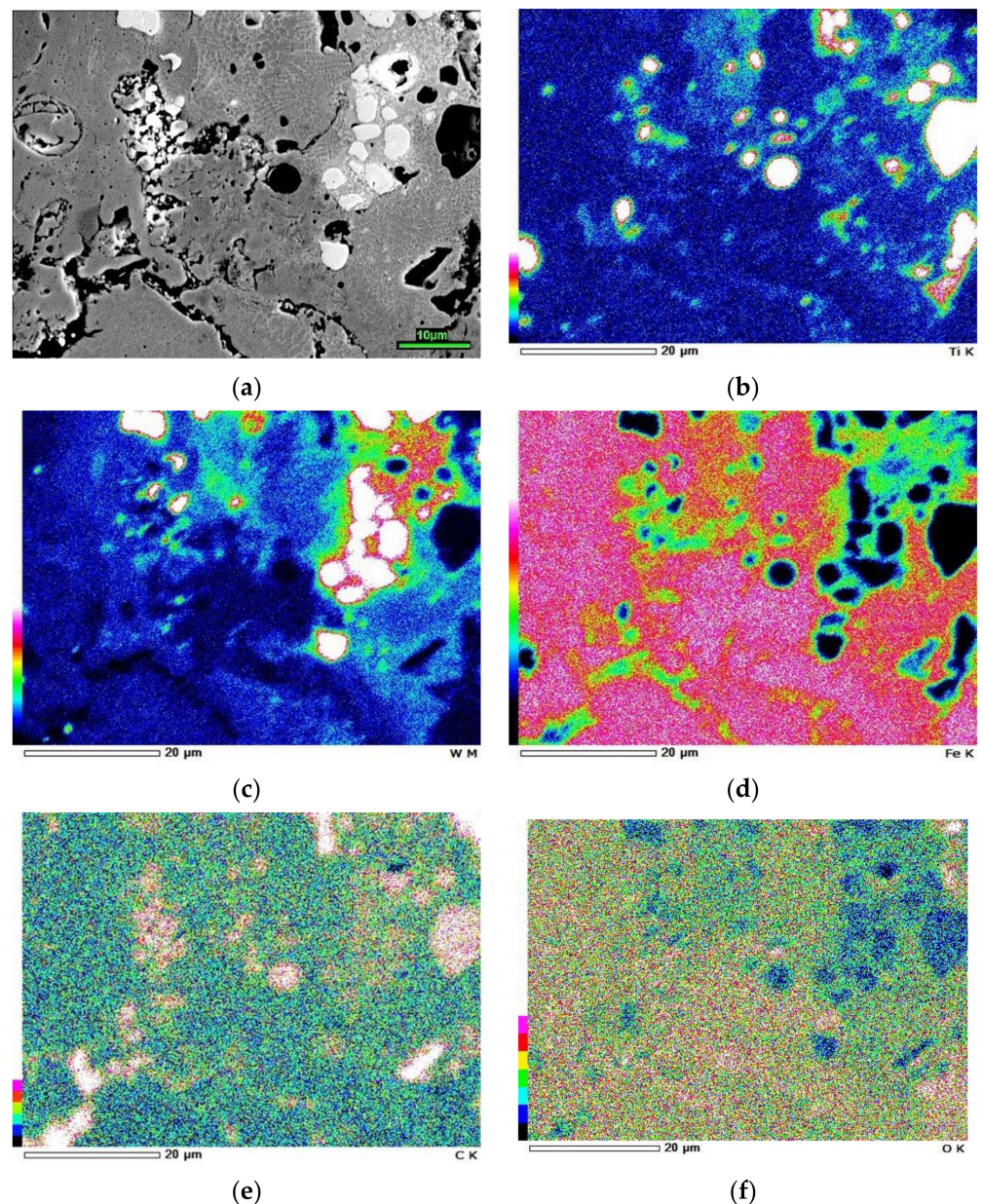
Figure 8. Elemental EDX-mapping of the coating: (**a**) SEM(BSEI), distribution of (**b**) Ti, (**c**) W, (**d**) Fe, (**e**) C, (**f**) O.

The mapping results were supported by elemental EDX-profiling. The results are shown in Figure 9, which presents the back-scattered electron images of two coatings' areas. Figure 9a illustrates the profiles of W, Ti, Fe, and C across the different carbides. Coarse carbides WC (point 004) and TiC (point 009) responded with sharp spikes in W and Ti concentration accompanied by a sharp drop in iron content. In contrast, the dotted conglomeration of smaller carbides had lower W/Ti profiles and a higher Fe profile. This behaviour was presumably due to (a) a smaller carbide size and (b) the presence of M_3C carbides having a lower amount of W and Ti.
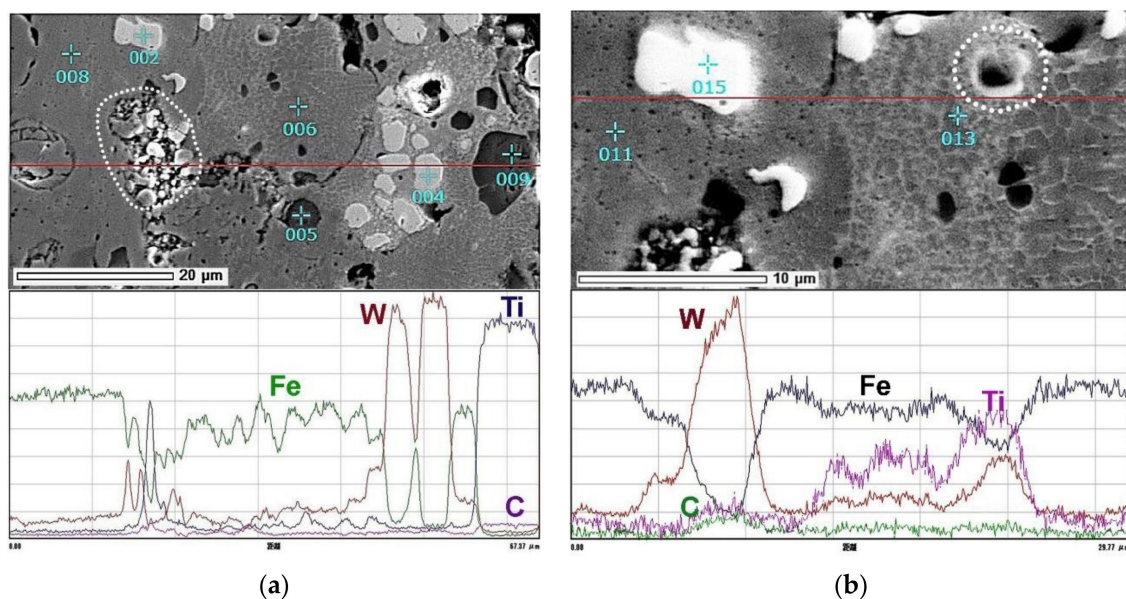
(**a**)   (**b**)

Figure 9. The EDX-profiles of C, W, Ti and Fe within the coating: (**a**) across WC and TiC carbides, (**b**) across carbide-free matrix and "carbide network" matrix.

More detailed information on elemental distribution in the matrix was derived from Figure 9b. As seen, the line crosses the carbide-free matrix (point 011) and the matrix with a carbide network (point 013). In the BSE image, the carbide network has bright coloration indicating its enrichment with the element of higher atomic number (tungsten). Tungsten profile through the "carbide network matrix" area exhibited a higher level as compared to carbide-free matrix area, proving its enrichment by tungsten. The same behaviour was noted for the titanium profile which follows the tungsten profile. The dotted particle crossed by a line draws special attention: it is a titanium carbide (dark) surrounded by a W-rich matrix edge (bright). Therefore, this particle attracts the spikes of W and Ti both.

The phase chemical composition of the coating has been clarified using a local EDX-analysis and summarized in Table 1 (the indicative analyzed points are designated in Figure 9). The bright-contrast precipitates contained 89.5 wt.% W, 7.8 wt.% C, and 2.7 wt.% Fe, which is close to tungsten monocarbide WC stoichiometry (93.9 wt.% W, and 6.1 wt.% C). The dark-contrast particles had a composition (77.6 wt.% Ti, 17.5 wt.% C, 4.3 wt.% Fe, and 0.7 wt.% W) revealing them as titanium carbide TiC (stoichiometric composition is 80 wt.% Ti and 20 wt.% C). Impurity elements found in carbides (iron in WC and TiC; tungsten in TiC) were presumably absorbed due to plasma-chemical reactions in plasma flow. The features of EDX-spectra for different carbides are shown in Figure 10a,b.

Table 1. Phase chemical composition of the coating.

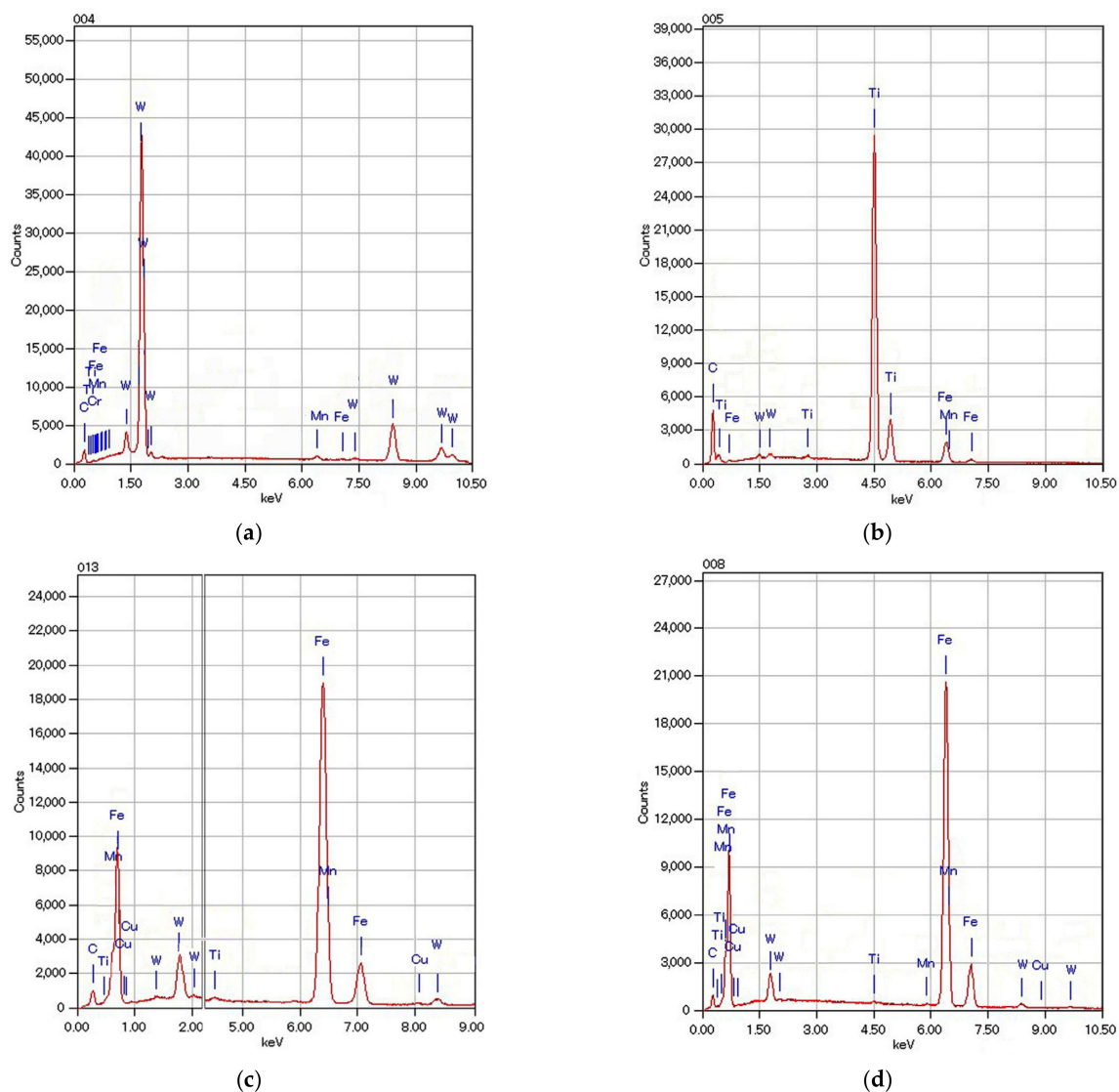| Phase	Elements (wt.%)				
	C	Ti	W	Cu	Fe
WC	7.79 ± 1.91	-	89.53 ± 0.82	-	2.67 ± 0.79
TiC	17.46 ± 3.65	77.57 ± 6.92	0.72 ± 0.43	-	4.25 ± 3.02
Carbide-free matrix	5.95 ± 0.89	0.37 ± 0.06	11.26 ± 1.28	0.77 ± 0.24	81.25 ± 1.93
"Carbide network" matrix	8.76 ± 0.70	3.32 ± 1.07	16.98 ± 2.02	1.06 ± 0.05	74.72 ± 2.86

Figure 10. EDX-spectra for the indicative points shown in Figure 8: (**a**) WC carbide (point 004), (**b**) TiC carbide (point 005), (**c**) "carbide network"-matrix (point 013), (**d**) carbide-free matrix (point 008).

Considering the spotty character of a matrix's structure, EDX point analysis was performed on homogenous areas (the point 008 in Figure 9a and the point 011 in Figure 9b) and on "carbide network" areas (the point 006 in Figure 9a and the point 013 in Figure 9b). The major element in both cases was iron (about 80 wt.%); Ti, W, and Cu were also detected in both areas as well. The "matrix/carbide network" responded higher amounts of C, W, and Ti (Figure 10c), which was affected by the carbide net. Since a spatial resolution of EDX beam was 2–3 μm, the analyzed spot included both matrix phase and carbide network, thus the latter contributed to EDX results. Carbide-free matrix had lower amount of C, W (by 1.5 times), and Ti (by 10 times) and a slightly higher content of copper (Figure 10d). Carbon content measured in matrix (6–8.7 wt.%) is considered as excessive due to the high sensitivity of the EDX method to carbon contamination [60].

3.2. Tribological Behaviour Evaluation

The tribological properties of the coating were evaluated in comparison with the substrate (steel of AISI 4145H grade). Variation of CoF during the sliding test is shown in Figure 11. When sliding against the steel ball, the substrate performed with the highest coefficient of friction: after a running-in period, the mean CoF value was 0.62 (Figure 11a). The coating responded with a lower mean CoF value (0.52). The sliding against the SiC

ball was characterized by much lower friction force for both the substrate and the coating: the mean coefficient of friction for the substrate reached 0.43, while the coating exhibited CoF = 0.10 (Figure 11b).
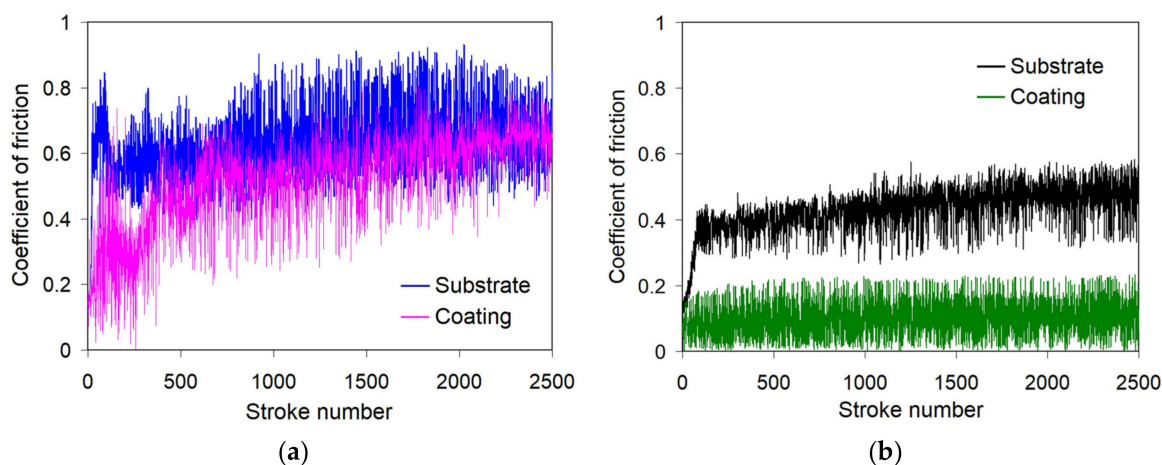

Figure 11. Variation of a mean CoF value during the wear test: (**a**) sliding against 100Cr6 ball, (**b**) sliding against SiC ball.

According to CoF variation, the wear tracks of different sliding couples significantly varied in their width and depth (as shown in Figure 12). As follows from 3D images, the tracks on the substrate (Figure 12a,b) were much larger in width and depth than that of the coating (Figure 12c,d). The comparison of wear track profiles, presented in Figure 12e, reveals that sliding against the 100Cr6 counter-body resulted in wider and deeper wear tracks than that of SiC. An especially large track (300 μm wide and 0.8 μm deep) was ploughed by the steel ball on the substrate (steel of AISI 4145H grade) surface; the wear track on the coating surface was twice as shallow. The sliding against a silicon carbide ball produced more shallow tracks with a depth of 0.17 μm on the substrate surface and 0.05 μm on the coating surface.

The difference in friction behaviour resulted in the wear responses presented in Figure 12f. As seen, the highest volumetric wear (2718 $\mu m^3 \cdot N^{-1} \cdot m^{-1}$) was demonstrated by the substrate after sliding against the 100Cr6 counter-body. The substrate's volumetric wear was three times lower (~730 $\mu m^3 \cdot N^{-1} \cdot m^{-1}$) when in contact with a SiC ball. As compared with the substrate, the coating had better wear resistance which manifested in decreasing the ΔV value to 621 $\mu m^3 \cdot N^{-1} \cdot m^{-1}$ (sliding against a 100Cr6 ball) and to ~46 $\mu m^3 \cdot N^{-1} \cdot m^{-1}$ (sliding against a SiC ball).

As follows from Figure 13, the wear testing affected a counter ball's surface. As seen, for each sliding couple the wear spot appeared on the ball surface surrounded by the wear debris. The largest spot area (275.4 × 10^{-3} μm²) was attributed to the steel ball after sliding against the coating (Figure 13e). After testing against the substrate, the spot area on the steel ball was also rather high—202.4 × 10^{-3} μm². In contrast, the SiC ball featured a much lower spot area with a minimal value (30.8 × 10^{-3} μm²) after sliding against the coating. After removing the debris from the balls' surfaces, it was found that the wear spots on 100Cr6 steel balls were flat with parallel grooves that appeared due to the ball wear-off (Figure 13a,c). The wear spots on SiC balls had a curvilinear shape; the wear spots were only noticeable owing to the traces of the adhered wear debris (Figure 13b,d).
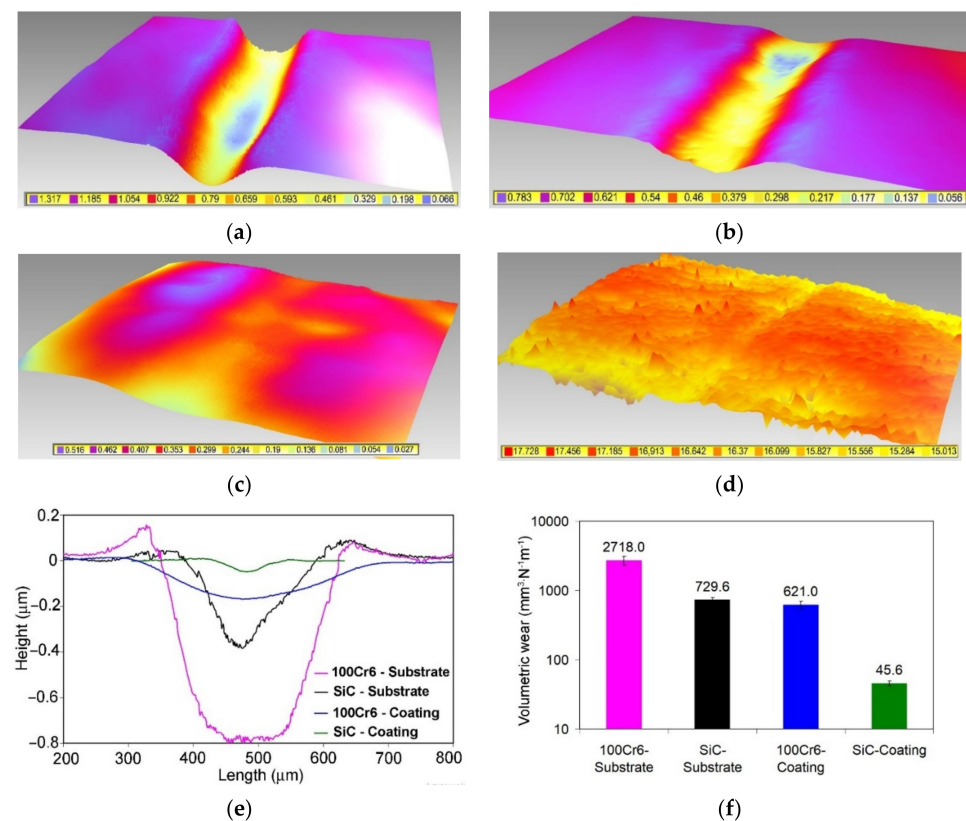
Figure 12. 3D images of the wear tracks for different sliding couples: (**a**) 100Cr6-substrate (steel of AISI 4145H grade), (**b**) SiC-substrate (steel of AISI 4145H grade), (**c**) 100Cr6-coating, (**d**) SiC-coating. Dry-sliding wear characteristics of the specimens: (**e**) wear track profiles, and (**f**) volumetric wear (The values of a profile height in Figure (**a**–**d**) are given in μm).
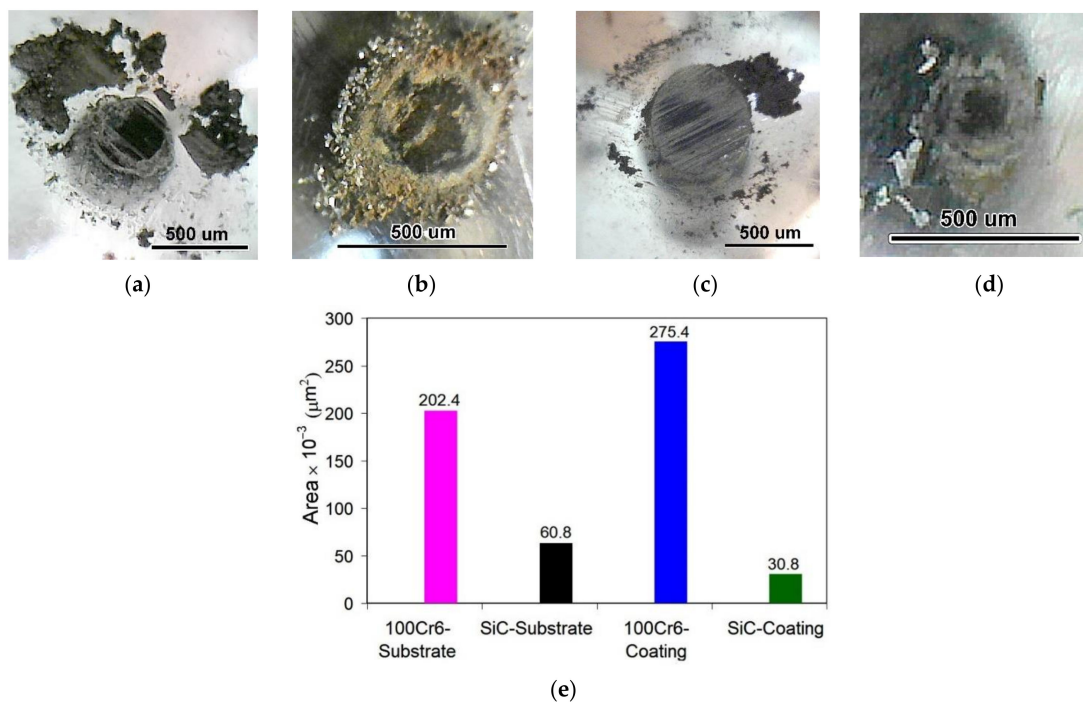

Figure 13. Worn surface of the counter balls: (**a**) 100Cr6-substrate (steel of AISI 4145H grade), (**b**) SiC-substrate (steel of AISI 4145H grade), (**c**) 100Cr6-coating, (**d**) SiC-coating.(**e**) Mean surface area of the wear spot on the ball after sliding test.
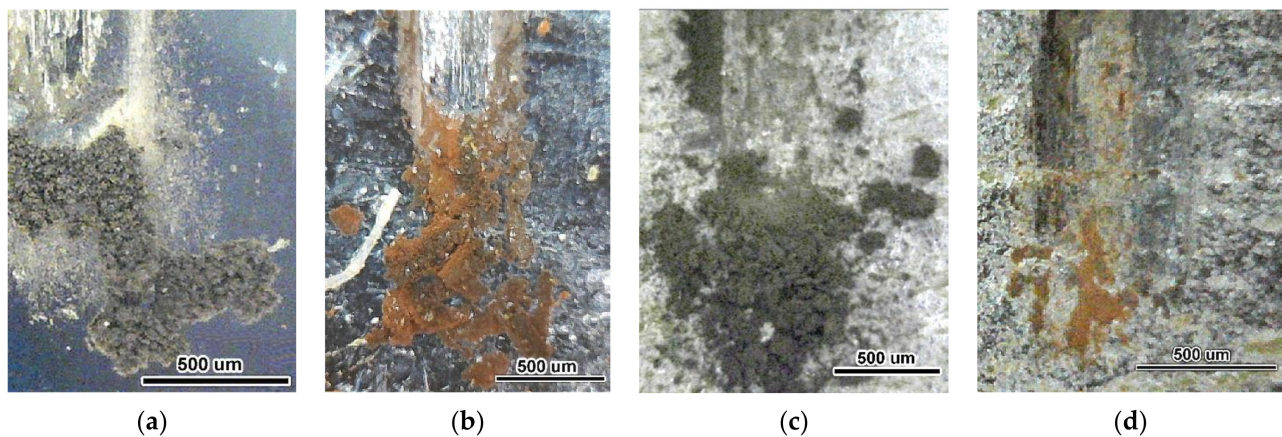
Figure 14. Optical micrographs of the wear debris for different sliding couples: (**a**) 100Cr6-substrate (steel of AISI 4145H grade), (**b**) SiC-substrate (steel of AISI 4145H grade), (**c**) 100Cr6-coating, (**d**) SiC-coating.
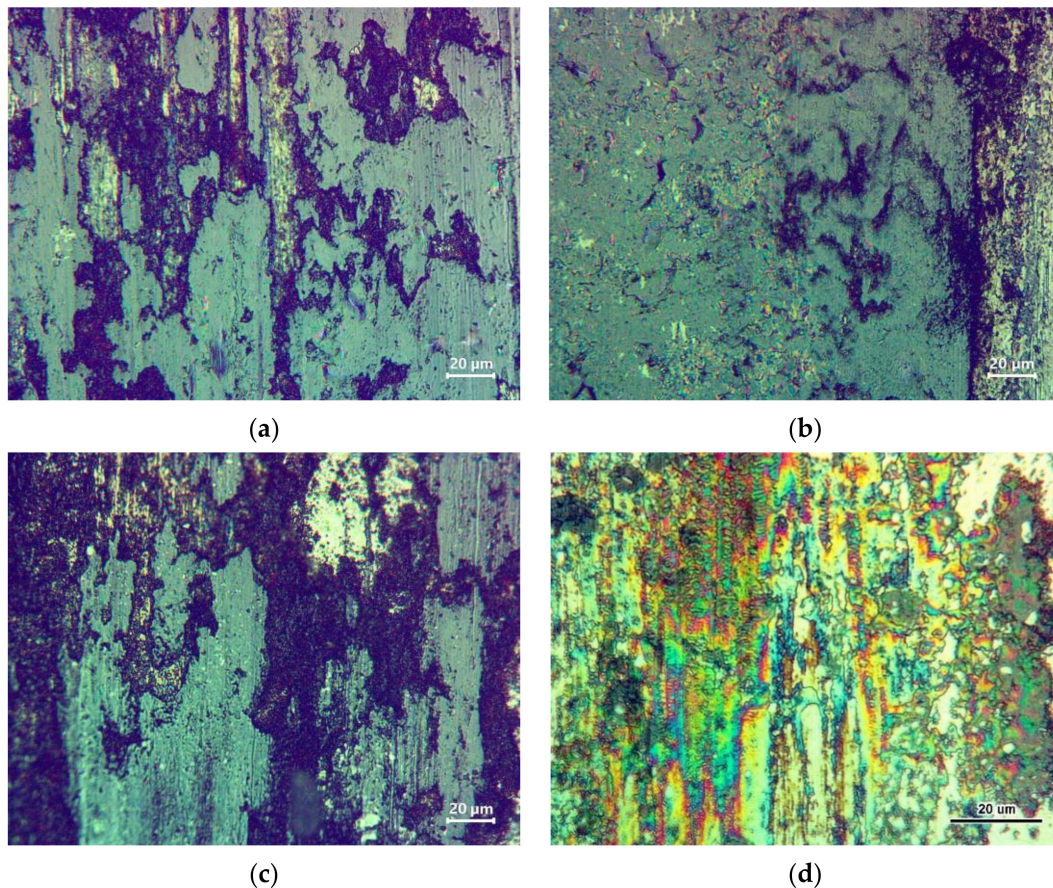

Figure 15. Oxide films on the worn surface of the specimens: (**a**) 100Cr6-substrate (steel of AISI 4145H grade), (**b**) SiC-substrate (steel of AISI 4145H grade), (**c**) 100Cr6-coating, (**d**) SiC-coating.

The wear debris was accumulated at the edges of the wear track (Figure 14). Sliding against a 100Cr6 ball resulted in powdered debris of dark-grey colour (Figure 14a,c). Unlike this, the debris that formed after sliding against the SiC ball was of bright reddish colour, having a petal-like shape. A difference in the nature of the wear products indicates the obvious dissimilarity in the mechanism of the specimen's wear depending on the material of the counter-body. This assumption is supported by the appearance of the wear tracks shown in Figure 15. As follows from Figure 15b, in sliding couple "SiC-substrate" the wear

track was covered with a dense continuous oxide scale (with not numerous cracks within the scale). The dark colour of the scale indicated the high temperature that occurred in near-surface layers under the sliding. The same thick oxide scales were also characteristic for the wear tracks formed under sliding against a 100Cr6 steel ball, although in these cases the scales were discontinuous: they were interspersed with the dark-contrast areas of the scale spalling and the light-contrast areas of non-oxidized surface (Figure 15b,c). When SiC balls slid against the coating, the wear track was entirely covered with a thin continuous oxide scale; due to its low thickness the scale was transparent, allowing the light beam interference manifestation (Figure 15d).

4. Discussion

The performed studies have shown that, using the proposed design of the cathode and the parameters of pulse-plasma deposition, it is possible to form a composite coating by direct deposition of carbides without their melting. This became possible due to the processes occurring inside the EAPA chamber during electrical discharge. The main in these processes is: (a) the burnout of the epoxy resin bond and the release of carbide particles (enabling their plasma-transfer to the surface) and (b) the formation of a high-carbon metal matrix due to the plasma-saturation of iron with carbon, which ensures the obtaining of high-carbon (hard) martensite in the matrix structure.

Comparison of the amount and size of carbides in the filler of the cathode and in the coating shows the closeness of their particle volume fraction and size distribution. This indicates that the carbides were delivered to the surface in their original state, i.e., in a non-molten state. This conclusion should be specified in a view of Ti and W presence on the matrix revealed by EDX-analyzing (Table 1, Figure 10c,d). The dissolution of some titanium and tungsten in the matrix is clearly seen in Figure 8b,c showing the halos surrounding the carbide particles that are the matrix areas enriched by Ti or W. One can speculate that partial melting of TiC/WC particles took place under pulsed-plasma deposition with corresponding Ti/W enrichment of a melt around the particles.

Another source of Ti/W atoms could be the TiC/WC carbides evaporated (together with iron) in the cathode spot in direct contact with an electric arc. The released Ti, W, and Fe atoms fell into the plasma flow and were transferred to the surface. Those atoms were presumably partially absorbed by the carbide particles in-flight, which follows from the presence of W and Fe in TiC carbides and Fe—in WC carbides (Table 1). The presence of copper in the coating's matrix (0.8–1.0 wt.%) is also attributed to the plasma transfer of Cu atoms evaporated on the surface of the cathode copper mount. The matrix areas oversaturated with Ti and W enrichment crystallized through precipitation of (Fe, W, and Ti)$_3$C carbide network along the matrix grain boundaries. The areas with moderate Ti/W content remained non-decomposed being frozen under superfast coating crystallization (the cooling velocity of pulsed-plasma coating was estimated as 10^6–10^7 K·s^{-1} in [48]).

The microstructural study allowed to conclude that PPT in the air atmosphere was accompanied by the oxidation of the products of the EAPA electrodes' erosion (carbides and liquid steel microdrops). The oxidation of the carbides was evidenced by the oxide inclusions present at the carbide/matrix boundaries. The oxidation of the molten steel microdrops was revealed by the extended oxide films not closely associated with the carbides. Similar phenomena (oxidation and decarburization) were described regarding the thermal spraying of WC carbides [61]. The presence of oxide film might negatively affect the mechanical properties of the coating and its resistance to abrasive wears, though in the case of dry-sliding applications the oxide films can be useful, serving as solid lubricants. Carbide/steel oxidation was obviously caused by the interaction with atmospheric oxygen, although it also could be enhanced by the gaseous combustion products of epoxy burning. According to [62], high-temperature combustion and pyrolysis of the epoxy polymer results in the emissions of different gases (CO_2, CO, H_2O, aliphatic hydrocarbons, etc.), some of which are oxidizing agents. This requires further research to find a proper binder for the cathode's filler in order to avoid excessive oxide contamination of the coating.

High hardness and acicular pattern of the matrix revealed the presence of high-carbon plate martensite in the PMMC matrix. Most microhardness measurements fell into the interval of 700–800 HV, being equivalent to 60–64 HRC typical for a cutting tool made of high-speed steel. A minor part of the measurements was below 700 HV, referring to the mixture of martensite and retained austenite. As it was derived from the XRD pattern, the martensite was only about half of the matrix volume; the rest of the volume was occupied by austenite. The high volume fraction of RA was a result of the coating's enrichment with carbon. Austenite was retained in matrix areas enriched with carbon up to 1.43 wt.% (as follows from XRD pattern). Austenite/martensite volume ratio depends on Ms temperature that can be calculated by Payson and Savage's [63] equation:

$$Ms = 499 - 308 \cdot C - 32.4 \cdot Mn - 27 \cdot Cr - 16.2 \cdot Ni - 10.8 \cdot (Si + Mo + W) - 16.3 \cdot Cu + 10.8 \cdot Ti, \quad (4)$$

where C, Mn, Cr, Ni, Si, Mo, W, Cu, and Ti are the contents of the elements (wt.%) in matrix.

The last two terms were added to Equation (4), being adopted from Barbier's equation [64] in order to use Equation (4) for calculation of Ms for the coating's matrix. Carbon content was assumed as 1.43 wt.%, and other elements' (W, Cu, and Ti) contents were taken from Table 1, for carbide-free matrix. Ms was calculated as minus 82.7 °C, proving a fully austenitic structure in carbon-enriched areas of the matrix. At the same time, the presence of martensite in the coating's matrix implies that the average Ms value was higher than room temperature.

The average *Ms* value for the coating can be derived from the Koistinen–Marburger equation:

$$f_M = 1 - \exp(-a_m(Ms - TQ)), \quad (5)$$

where f_M is a martensite volume fraction at quenching temperature *TQ* (20 °C), a_m is a fitting coefficient ($a_m = 0.008$ for Fe − 1.86 wt.% C alloy [65]).

Assuming $f_M = 0.43$ for the coating's matrix (according to XRD pattern), the average Ms temperature was found as 90.8 °C, which corresponds to the average carbon content of 0.865 wt.% C (by Equation (4)). This means that carbon content in martensite should be 0.13 wt.% to balance with the carbon content in RA (1.43 wt.%) (regarding the RA/martensite volume ratio). However, the high microhardness measured in the matrix implies much higher carbon content in the martensite. This means that the actual carbon content in the coating's matrix varies in very wide limits, making a heterogeneous matrix with a variation of structural states from "low-carbon lath martensite (soft)" to "high-carbon plate martensite (hard)" and to "high-carbon retained austenite (soft)". One can presume that exactly the "carbide network" matrix areas had a mostly martensitic structure due to depletion by carbon and alloying elements that occurred through the carbide network formation. Conversely, the carbide-free matrix areas are supposedly austenite stabilized by dissolved carbon and other elements. According to [66,67] the heterogeneous matrix is beneficial for wear-resistant materials due to better adaptability and redistribution of the stresses that occurred in contact with abrasive particles. Moreover, it can be assumed that RA in a PMMC coating partially transforms to martensite under wear testing, contributing to wear resistance via TRIP-effect [68].

The data presented in Figures 12–15 give insight to the mechanism of the specimens' wear. The sliding on the substrate surface caused intensive friction with a deep and wide groove formation. The sliding of the 100Cr6 steel ball resulted in protrusions on both sides of the wear track, which is characteristic for the abrasion of the soft materials. With the ball deepening, the contact area increased and an abrasion transformed into intensive deformation of the near-surface layers of the substrate, accompanied by their heating and dynamic oxidation with a thick oxide scale formation (Figure 15). Oxide scale protected the surface, reducing the friction force and inhibiting the plasticity-dominated mechanisms; however, the repetitive sliding resulted in deterioration and delamination of the oxide scale with eventual debris formation as shown in Figures 13 and 14. Thus, the main wear mechanism after a running-in period for all sliding couples was dry oxidative wear [69].

It is noteworthy that sliding of the steel ball produced a much higher surface deterioration of the substrate/coating surface as compared to the SiC ball (despite the increased hardness of the latter). This can be explained by the proximity of the crystal structure of the steel ball and the substrate which facilitates the interatomic interaction in a contact spot, causing the adhesion with a galling manifestation [70,71]. As seen in Figure 15a, the oxide film on the substrate after sliding against the steel ball was discontinuous; thus, it could not fully protect the surface from the adhesion with the counter ball surface. This allowed speculation that after sliding against the 100Cr steel ball the debris consisted of the oxide chips and the products of galling. In contrast, SiC had a hexagonal crystal lattice that suppressed its adhesion with a cubic lattice of the substrate (BCC). Inhibiting adhesion benefited the decrease in coefficient of friction (Figure 11) and volumetric wear (Figure 12f). Therefore, the sliding of SiC over a steel surface responded only by deformation/oxidation behaviour where the oxidation presumably was more intensive than that of the steel ball sliding. An intensive oxidation led to the formation of a more durable oxide scale with a higher protective potential. This assumption was supported by the micrograph of the wear track of the "SiC-substrate" couple (Figure 15b) showing the dense continuous oxide scale which tightly covered entire the surface of the wear track. The oxide films that emerged under the SiC ball sliding differed in structure/chemical composition from those of the sliding against the 100Cr steel ball. This follows from the different colour and the shape of the wear debris, which were "dark-grey/powdered" for the steel ball and "reddish/petal-shaped"—for the SiC ball (Figure 14). However, it is necessary to keep in mind that the colour of the debris might be affected by the products of the ball's wear.

Under the sliding, the protective oxide films acted as the abrasive agents abrading the counter ball surface. The steel balls were affected to more extent that manifested in the formation on their surface a flat worn spot covered by the parallel grooves (Figure 13a,c). The spot area was the highest for the "100Cr6-coating" couple. The increase in spot area in this case is explained by the contribution of WC/TiC carbides (present in the coating structure) into the abrading of the steel ball surface. The higher rate of steel ball flattening resulted in wide and shallow wear track characteristics for the "100Cr6-coating" couple (Figure 12e). In contrast, the surface of SiC balls was negligibly affected by the sliding regardless of the counter surface material: only the slight adhering of wear debris was noted without surface flattening. The high wear resistance of the SiC ball was due to its extremely high hardness (2600 HV). The maintaining of the spherical shape of the SiC ball during the testing led to a lower width of the wear tracks as compared with the flattened steel ball. This also ensured the constancy of high stress in contact with the specimen, promoting a higher rate of the "deformation-heating-oxidation" process with the dense protective oxide formation. Unlike this, the fast flattening of the steel ball decreased the contact stress which resulted in a less-dense discontinuous oxide scale with lower protective ability.

The coating performed an undisputable advantage in the tribological properties as compared to the substrate (steel of AISI 4145H grade). An increased hardness (due to carbide particulates and hardened matrix) minimized the coating surface deformation when contacting the steel ball; therefore, the galling effect was suppressed, resulting in a lower coefficient of friction. The decrease in CoF was additionally enabled by the oxide films (TiO_2, WO_2, and WO_3) revealed in the coating's structure and confirmed by X-ray diffraction. Those oxides could act as a lubricant, inhibiting adhesion between the contacting surfaces [72,73]. However, the mean CoF for the "100Cr6-coating" was rather high (0.52) to be attributed to galling and abrasion of the ball surface by the carbide particles. Eventually, when testing with a 100Cr6 counter ball, the volumetric wear of the coating was 4.4 times lower than that of the substrate.

The tribological advantage of the coating manifested to a greater extent when sliding against SiC ball. The coating's mean CoF decreased to a minimal value (0.10) while its volumetric wear lowered by 16 times relatively the substrate. The wear of the couple "SiC-coating" was accompanied by thin oxide films formation and minimal volume of the wear debris. This behavior reflects the high potential of "(TiC + WC)/Hardened steel" PMMC

coating under the tribological contact with mineral particles (SiO_2, Al_2O_3, SiC, etc.) which is the most common case for abrasive wear. It is worth noting what the described behaviour of the studied PMMC coating refers only to the used testing parameters (normal load, sliding speed and distance, etc.). A more deep understanding of the coating's performance in other wear conditions requires an extended tribological study.

This study revealed that the PPD/EAPA technique, using a consumable cathode of complex design, enables the direct fabrication of a PMMC coating with a hard matrix without performing an additional post-deposition heat treatment. The wear testing proved the high wear resistance of the coating in contact with different counter-body materials. Pulsed-plasma fabrication of PMMC coating can be prospective for wear applications when the protective coating should be of several tens of microns thickness. The optimization of phase/chemical composition and the ratio "carbide/binder" in the cathode filler regarding specific wear conditions is the topic of future research.

5. Conclusions

The microstructure and sliding wear performance of a particle reinforced metal matrix composite (PMMC) manufactured by atmospheric pulsed-plasma deposition on AISI 4145H steel using an electro-thermal axial plasma accelerator (EAPA) were investigated. The following conclusions can be drawn:

1. A composite coating "(TiC + WC)/Hardened matrix" of 24–31 μm thick was consolidated on the steel surface after 10 plasma pulsed with the discharge voltage of 4.0 kV and each discharge duration of 1 ms. Using the consumable cathode of a novel complex design (low-carbon plane steel tube filled with "TiC/WC + Epoxy resin" mixer) enables the direct formation of PMMC coating via plasma-transfer of carbides from the cathode to the substrate (steel of AISI 4145H grade)surface without their substantial melting.

2. It is shown that the formation of the coating's matrix occurred due to melt enrichment with carbon released upon epoxy resin burnout and EAPA inner walls (bakelite) evaporation under high-current arc discharge. This resulted in the PMMC matrix consisting of 43 vol.% of plate martensite and 57 vol.% of retained austenite (RA) with high carbon content in the latter (1.43 wt.%). In addition, partial melting/oxidation of TiC and WC particles occurred under the plasma transfer leading to oxide films (TiO_2, WO_2, WO_3) formation and matrix enrichment with Ti (up to 3.3 wt.%) and W (up to 17 wt.%). The latter caused the precipitation of $(Fe,W,Ti)_3C$ carbide network under the coating crystallization.

3. The high hardness of the matrix (500–1044 HV) and its heterogeneous character supported by the protective oxide films presence enabled the improved wear behaviour of pulsed-plasma PMMC under dry-sliding conditions. It performed a lower coefficient of friction and increased wear characteristics compared with the substrate (steel of AISI 4145H grade):
    -   by 4.4 times lower volumetric wear under sliding against hardened 100Cr6 steel ball;
    -   by 16 times lower volumetric wear under sliding against SiC ball.

4. The wear mechanisms of pulsed-plasma PMMC coating depended on the counter-body material to be: (a) dry oxidative wear and galling when sliding against 100Cr steel counter ball (proceeded through the formation/destruction of thick opaque discontinuous oxide scale on the coating surface), (b) dry oxidative wear when sliding against SiC ball (accompanied with the formation of thin transparent oxide scale entirely covering the wear track surface).

References

1. Bauri, R.; Yadav, D. *Metal Matrix Composites by Friction Stir Processing*; Elsevier: Amsterdam, The Netherlands, 2018; pp. 1–119. [CrossRef]
2. Samal, P.; Vundavilli, P.R.; Meher, A.; Mahapatra, M.M. Recent progress in aluminum metal matrix composites: A review on processing, mechanical and wear properties. *J. Manuf. Process.* **2020**, *59*, 131–152. [CrossRef]
3. Mechnik, V.A.; Bondarenko, N.A.; Kolodnitskyi, V.M.; Zakiev, V.I.; Zakiev, I.M.; Ignatovich, S.R.; Dub, S.N.; Kuzin, N.O. Effect of vacuum hot pressing temperature on the mechanical and tribological properties of the Fe-Cu-Ni-Sn-Vn composites. *Powder Metall. Met. Ceram.* **2020**, *58*, 679–691. [CrossRef]
4. Efremenko, V.G.; Shimizu, K.; Cheiliakh, A.P.; Kozarevs'ka, T.V.; Chabak, Y.G.; Hara, H.; Kusumoto, K. Abrasive wear resistance of spheroidal vanadium carbide cast irons. *J. Frict. Wear* **2013**, *34*, 466–474. [CrossRef]
5. Alpas, A.T.; Bhattacharya, S.; Hutchings, I.M. Wear of particulate metal matrix composites. In *Comprehensive Composite Materials II*; Beaumont, P.W.R., Zweben, C.H., Eds.; Elsevier: Amsterdam, The Netherlands, 2018; Volume 4, pp. 137–172. [CrossRef]
6. Bakkar, A.; Ahmed, M.M.Z.; Alsaleh, N.A.; Seleman, M.M.E.-S.; Ataya, S. Microstructure, wear, and corrosion characterization of high TiC content Inconel 625 matrix composites. *J. Mater. Res. Technol.* **2019**, *8*, 1102–1110. [CrossRef]
7. Sukhova, O.V.; Syrovatko, Y.V. New metallic materials and synthetic metals. *Metallofiz. Noveishie Tekhnologii* **2019**, *41*, 1171–1185. [CrossRef]
8. Pramanik, S.; Kar, K.K. Coating Technologies for Metal Matrix Composites. In *Encyclopedia of Materials: Composites*; Brabazon, D., Ed.; Elsevier: Amsterdam, The Netherlands, 2021; Volume 1, pp. 454–473. [CrossRef]
9. Kılıç, F.; Gül, H.; Aslan, S.; Alp, A.; Akbulut, H. Effect of CTAB concentration in the electrolyte on the tribological properties of nanoparticle SiC reinforced Ni metal matrix composite (MMC) coatings produced by electrodeposition. *Colloids Surf. A* **2013**, *419*, 53–60. [CrossRef]
10. Lee, Y.T.R.; Ashrafizadeh, H.; Fisher, G.; McDonald, A. Effect of type of reinforcing particles on the deposition efficiency and wear resistance of low-pressure cold-sprayed metal matrix composite coatings. *Surf. Coat. Technol.* **2017**, *324*, 190–200. [CrossRef]
11. Winnicki, M.; Łapa, W.; Znamirowski, Z. Field electron emission experiments with cold-sprayed Cu-SiC composite coatings. *Coatings* **2021**, *11*, 134. [CrossRef]
12. Xie, X.; Chen, C.; Chen, Z.; Addad, A.; Xie, Y.; Wu, X.; Verdy, C.; Wang, Y.; Wang, J.; Ren, Z.; et al. Effect of annealing treatment on microstructure and mechanical properties of cold sprayed TiB$_2$/AlSi$_{10}$Mg composites. *Surf. Interfaces* **2021**, *26*, 101341. [CrossRef]
13. Wang, W.; Zeng, X.; Li, Y.; Wang, D.; Liu, Y.; Yamaguchi, T.; Nishio, K.; Cao, J. Fabrication, microstructure, and wear performance of WC-Fe composite/metal coating fabricated by resistance seam welding. *Mater. Charact.* **2017**, *134*, 182–193. [CrossRef]
14. Farías, I.; Olmos, L.; Jiménez, O.; Flores, M.; Braem, A.; Vleugels, J. Wear modes in open porosity titanium matrix composites with TiC addition processed by spark plasma sintering. *Trans. Nonferrous Met. Soc. China* **2019**, *29*, 1653–1664. [CrossRef]
15. Cabezas-Villa, J.L.; Olmos, L.; Vergara-Hernández, H.J.; Jiménez, O.; Garnica, P.; Bouvard, D.; Flores, M. Constrained sintering and wear properties of Cu-WC composite coatings. *Trans. Nonferrous Met. Soc. China* **2017**, *27*, 2214–2224. [CrossRef]
16. Ziejewska, C.; Marczyk, J.; Szewczyk-Nykiel, A.; Nykiel, M.; Hebda, M. Influence of size and volume share of WC particles on the properties of sintered metal matrix composites. *Adv. Powder Technol.* **2019**, *30*, 835–842. [CrossRef]

17. Xu, J.; Zou, B.; Zhao, S.; Hui, Y.; Huang, W.; Zhou, X.; Wang, Y.; Cai, X.; Cao, X. Fabrication and properties of ZrC–ZrB$_2$/Ni cermet coatings on a magnesium alloy by atmospheric plasma spraying of SHS powders. *Ceram. Int.* **2014**, *40*, 15537–15544. [CrossRef]

18. Xu, L.; Song, J.; Zhang, X.; Deng, C.; Liu, M.; Zhou, K. Microstructure and corrosion resistance of WC-based cermet/Fe-based amorphous alloy composite coatings. *Coatings* **2018**, *8*, 393. [CrossRef]

19. Mordyuk, B.N.; Voloshko, S.M.; Zakiev, V.I.; Burmak, A.P.; Mohylko, V.V. Enhanced resistance of Ti6Al4V alloy to high-temperature oxidation and corrosion by forming alumina composite coating. *J. Mater. Eng. Perform.* **2021**, *30*, 1780–1795. [CrossRef]

20. Ostolaza, M.; Arrizubieta, J.I.; Cortina, M.; Lamikiz, A. Study of the reinforcement phase dilution into the metal matrix in functionally graded Stellite 6 and WC metal matrix composite by laser metal deposition. *Proc. CIRP* **2020**, *94*, 330–335. [CrossRef]

21. Duryagina, Z.A.; Bespalov, S.A.; Borysyuk, A.K.; Pidkova, V.Y. Magnetometric analysis of surface layers of 12X18H10T steel after ion-beam nitriding. *Metallofiz. Noveishie Tekhnologii* **2011**, *33*, 615–622.

22. Tang, B.; Tan, Y.; Xu, T.; Sun, Z.; Li, X. Effects of TiB2 particles content on microstructure, mechanical properties and tribological properties of Ni-based composite coatings reinforced with TiB2 particles by laser cladding. *Coatings* **2020**, *10*, 813. [CrossRef]

23. Kotarska, A.; Poloczek, T.; Janicki, D. Characterization of the structure, mechanical properties and erosive resistance of the laser cladded Inconel 625-based coatings reinforced by TiC particles. *Materials* **2021**, *14*, 2225. [CrossRef]

24. Li, Z.; Yan, H.; Zhang, P.; Guo, J.; Yu, Z.; Ringsberg, J.W. Improving surface resistance to wear and corrosion of nickel-aluminum bronze by laser-clad TaC/Co-based alloy composite coatings. *Surf. Coat. Technol.* **2021**, *405*, 126592. [CrossRef]

25. Tan, H.; Luo, Z.; Li, Y.; Yan, F.; Duan, R.; Huang, Y. Effect of strengthening particles on the dry sliding wear behavior of Al$_2$O$_3$–M$_7$C$_3$/Fe metal matrix composite coatings produced by laser cladding. *Wear* **2015**, *324–325*, 36–44. [CrossRef]

26. Peng, Y.; Zhang, W.; Li, T.; Zhang, M.; Liu, B.; Liu, Y.; Wang, L.; Hu, S. Effect of WC content on microstructures and mechanical properties of FeCoCrNi high-entropy alloy/WC composite coatings by plasma cladding. *Surf. Coat. Technol.* **2020**, *385*, 125326. [CrossRef]

27. Mashovets, N.S.; Pastukh, I.M.; Voloshko, S.M. Aspects of the practical application of titanium alloys after low temperature nitriding glow discharge in hydrogen-free-gas media. *Appl. Surf. Sci.* **2017**, *392*, 356–361. [CrossRef]

28. Oukach, S.; Pateyron, B.; Pawłowski, L. Physical and chemical phenomena occurring between solid ceramics and liquid metals and alloys at laser and plasma composite coatings formation: A review. *Surf. Sci. Rep.* **2019**, *74*, 213–241. [CrossRef]

29. Czupryński, A. Microstructure and abrasive wear resistance of metal matrix composite coatings deposited on steel grade AISI 4715 by powder plasma transferred arc welding part 1. Mechanical and structural properties of a cobalt-based alloy surface layer reinforced with particles of titanium carbide and synthetic metal–diamond composite. *Materials* **2021**, *14*, 2382. [CrossRef]

30. Zhang, X.; Cui, H.Z.; Wang, J.F.; Zhang, G.S.; Zhao, Y.Q.; Sun, K. Effects of TiB2 + TiC content on microstructure and wear resistance of Ni55-based composite coatings produced by plasma cladding. *Trans. Nonferrous Met. Soc. China* **2019**, *29*, 132–142. [CrossRef]

31. Rokanopoulou, A.; Skarvelis, P.; Papadimitriou, G.D. Improvement of the tribological properties of Al$_2$O$_3$ reinforced duplex stainless steel MMC coating by the addition of TiS$_2$ powder. *Surf. Coat. Technol.* **2016**, *289*, 144–149. [CrossRef]

32. Huang, Z.; Hou, Q.; Wang, P. Microstructure and properties of Cr$_3$C$_2$-modified nickel-based alloy coating deposited by plasma transferred arc process. *Surf. Coat. Technol.* **2008**, *202*, 2993–2999. [CrossRef]

33. Sivkov, A.; Shanenkov, I.; Pak, A.; Gerasimov, D.; Shanenkova, Y. Deposition of a TiC/Ti coating with a strong substrate adhesion using a high-speed plasma jet. *Surf. Coat. Technol.* **2016**, *291*, 1–6. [CrossRef]

34. Kovaleva, M.; Tyurin, Y.; Vasilik, N.; Kolisnichenko, O.; Prozorova, M.; Arseenko, M.; Yapryntsev, M.; Sirota, V.; Pavlenko, I. Effect of processing parameters on the microstructure and properties of WC–10Co–4Cr coatings formed by a new multi-chamber gas-dynamic accelerator. *Ceram. Int.* **2015**, *41*, 15067–15074. [CrossRef]

35. Kovaleva, M.G.; Goncharov, I.Y.; Novikov, V.Y.; Pavlenko, I.A.; Yapryntsev, M.N.; Vagina, O.N.; Sirota, V.V.; Tyurin, Y.N.; Kolisnichenko, O.V. Dense ZrB2-MoSi2 composite coating fabricated by a new multi- chamber detonation accelerator on carbon/carbon composites. *Mater. Sci. Forum* **2020**, *987*, 53–58. [CrossRef]

36. Rosinski, M.; Fortuna, E.; Michalski, A.; Pakiela, Z.; Kurzydlowski, K.J. W/Cu composites produced by pulse plasma sintering technique (PPS). *Fusion Eng. Des.* **2007**, *82*, 2621–2626. [CrossRef]

37. Darabara, M.; Papadimitriou, G.D.; Bourithis, L. Production of Fe–B–TiB$_2$ metal matrix composites on steel surface. *Surf. Coat. Technol.* **2006**, *201*, 3518–3523. [CrossRef]

38. Efremenko, B.; Belik, A.; Chabak, Y.; Halfa, H. Simulation of structure formation in the Fe–C–Cr–Ni–Si surfacing materials. *East.-Eur. J. Enterp. Technol.* **2018**, *2*, 33–38. [CrossRef]

39. Salloom, R.; Joshi, S.S.; Dahotre, N.B.; Srinivasan, S.G. Laser surface engineering of B$_4$C/Fe nano composite coating on low carbon steel: Experimental coupled with computational approach. *Mater. Des.* **2020**, *190*, 108576. [CrossRef]

40. Zhang, Z.; Kovacevic, R. Laser cladding of iron-based erosion resistant metal matrix composites. *J. Manuf. Process.* **2019**, *38*, 63–75. [CrossRef]

41. Chen, H.; Lu, Y.; Sun, Y.; Wei, Y.; Wang, X.; Liu, D. Coarse TiC particles reinforced H13 steel matrix composites produced by laser cladding. *Surf. Coat. Technol.* **2020**, *395*, 125867. [CrossRef]

42. Jiang, W.H.; Kovacevic, R. Laser deposited TiC/H13 tool steel composite coatings and their erosion resistance. *J. Mater. Process. Technol.* **2007**, *186*, 331–338. [CrossRef]

43. Gordo, E.; Velasco, F.; Antón, N.; Torralba, J.M. Wear mechanisms in high speed steel reinforced with (NbC)p and (TaC)p MMCs. *Wear* **2000**, *239*, 251–259. [CrossRef]

44. Kolyada, Y.E.; Fedun, V.I.; Tyutyunnikov, V.I.; Savinkov, N.A.; Kapustin, A.E. Formation mechanism of the metallic nanostructures using pulsed axial electrothermal plasma accelerator. *Probl. At. Sci. Technol.* **2013**, *86*, 297–300.

45. Kolyada, Y.E.; Bizyukov, A.A.; Bulanchuk, O.N.; Fedun, V.I. Pulse electrothermal plasma accelerators and its application in the technologies. *Probl. At. Sci. Technol.* **2015**, *98*, 319–324.

46. Efremenko, V.G.; Chabak, Y.G.; Lekatou, A.; Karantzalis, A.E.; Shimizu, K.; Fedun, V.I.; Azarkhov, A.Y.; Efremenko, A.V. Pulsed plasma deposition of Fe-C-Cr-W coating on high-Cr-cast iron: Effect of layered morphology and heat treatment on the microstructure and hardness. *Surf. Coat. Technol.* **2016**, *304*, 293–305. [CrossRef]

47. Chabak, Y.G.; Fedun, V.I.; Shimizu, K.; Efremenko, V.G.; Zurnadzhy, V.I. Phase-structural composition of coating obtained by pulsed plasma treatment using eroded cathode of T1 high speed steel. *Probl. At. Sci. Technol.* **2016**, *4*, 100–106.

48. Efremenko, V.G.; Chabak, Y.G.; Fedun, V.I.; Shimizu, K.; Pastukhova, T.V.; Petryshynets, I.; Zusin, A.M.; Kudinova, E.V.; Efremenko, B.V. Formation mechanism, microstructural features and dry-sliding behaviour of "Bronze/WC carbide" composite synthesised by atmospheric pulsed-plasma deposition. *Vacuum* **2021**, *185*, 110031. [CrossRef]

49. Kolyada, Y.E.; Fedun, V.I.; Onishchenko, I.N.; Kornilov, E.A. The use of a magnetic switch for commutation of high-current pulse circuits. *Instrum. Exp. Tech.* **2001**, *44*, 213–214. [CrossRef]

50. Chabak, Y.G.; Efremenko, V.G.; Shimizu, K.; Lekatou, A.; Pastukhova, T.V.; Azarkhov, A.Y.; Zurnadzhy, V.I. Comparative analysis of the microstructural features of 28 wt.% Cr cast iron fabricated by pulsed plasma deposition and conventional casting. *J. Mater. Eng. Perform.* **2018**, *27*, 379–388. [CrossRef]

51. Vander Voort, G.F. *Metallography, Principles and Practice*; ASTM International: West Conshohocken, PA, USA, 1999; pp. 1–752.

52. Buketov, A.; Brailo, M.; Yakushchenko, S.; Sapronova, A. Development of epoxy-polyester composite with improved thermophysical properties for restoration of details of sea and river transport. *Adv. Mater. Sci. Eng.* **2018**, *2018*, 6378782. [CrossRef]

53. Atta, A.M.; Ahmed, M.A.; El-Saeed, A.M.; Abo-Elenien, O.M.; El-Sockary, M.A. Hybrid ZrO_2/Cr_2O_3 epoxy nanocomposites as organic coatings for steel. *Coatings* **2020**, *10*, 997. [CrossRef]

54. Chabak, Y.G.; Fedun, V.I.; Pastukhova, T.V.; Zurnadzhy, V.I.; Berezhnyy, S.P.; Efremenko, V.G. Modification of steel surface by pulsed plasma heating. *Probl. At. Sci. Technol.* **2017**, *110*, 97–102.

55. Sun, J.; Hao, Y. Microstructure development and mechanical properties of quenching and partitioning (Q&P) steel and an incorporation of hot-dipping galvanization during Q&P process. *Mater. Sci. Eng. A* **2013**, *586*, 100–107. [CrossRef]

56. Van Dijk, N.H.; Butt, A.M.; Zhao, L.; Sietsma, J.; Offerman, S.E.; Wright, J.P.; van der Zwaag, S. Thermal stability of retained austenite in TRIP steels studied by synchrotron X-ray diffraction during cooling. *Acta Mater.* **2005**, *53*, 5439–5447. [CrossRef]

57. Berglund, K.; Rodiouchkina, M.; Hardell, J.; Kalliorinne, K.; Johansson, J. A Novel reciprocating tribometer for friction and wear measurements with high contact pressure and large area contact configurations. *Lubricants* **2021**, *9*, 123. [CrossRef]

58. Stormvinter, A.; Borgenstam, A.; Hedström, P. Investigation of lath and plate martensite in a carbon steel. *Solid State Phenom.* **2011**, *172–174*, 61–66. [CrossRef]

59. Kurlov, A.S.; Gusev, A.I. *Tungsten Carbides: Structure, Properties and Application in Hardmetal*; Springer Science & Business Media: Cham, Switzerland, 2013; pp. 1–242. [CrossRef]

60. Rolland, P.; Carlino, V.L.; Vane, R. Improved carbon analysis with evactron plasma cleaning. *Microsc. Microanal.* **2004**, *10*, 964–965. [CrossRef]

61. Yuan, J.; Zhan, Q.; Huang, J.; Ding, S.; Li, H. Decarburization mechanisms of WC–Co during thermal spraying: Insights from controlled carbon loss and microstructure characterization. *Mater. Chem. Phys.* **2013**, *142*, 165–171. [CrossRef]

62. Tansir, A.; Alshehri, S. Thermal degradation and evolved gas analysis of epoxy (DGEBA)/novolac resin blends (ENB) during pyrolysis and combustion. *J. Therm. Anal. Calorim.* **2012**, *111*, 445–451. [CrossRef]

63. Payson, P.; Savage, C.H. Martensite reactions in alloy steels. *Trans. ASM* **1944**, *33*, 261–280.

64. Barbier, D. Extension of the martensite transformation temperature relation to larger alloying elements and contents. *Adv. Eng. Mater.* **2014**, *1*, 122–127. [CrossRef]

65. Mendiratta, M.G.; Krauss, G. The development of martensitic microstructure and microcracking in an Fe-1.86 C alloy. *Metall. Mater. Trans. B* **1972**, *3*, 1755–1760. [CrossRef]

66. Malinov, L.S.; Malysheva, I.E.; Klimov, E.S.; Kukhar, V.V.; Balalayeva, E. Effect of particular combinations of quenching, tempering and carburization on abrasive wear of low-carbon manganese steels with metastable austenite. *Mater. Sci. Forum* **2019**, *945*, 574–578. [CrossRef]

67. Golyshev, A.A.; Malikov, A.G.; Orishich, A.M. The formation of heterogeneous wear-resistant coatings by the additive technology method. *J. Phys. Conf. Ser.* **2019**, *1404*, 012019. [CrossRef]

68. Efremenko, V.G.; Shimizu, K.; Cheiliakh, A.P.; Pastukhova, T.V.; Chabak, Y.G.; Kusumoto, K. Abrasive resistance of metastable V–Cr–Mn–Ni spheroidal carbide cast irons using the factorial design method. *Int. J. Miner. Metall. Mater.* **2016**, *23*, 645–657. [CrossRef]

69. Hutchings, I.; Shipway, P. *Tribology: Friction and Wear of Engineering Materials*, 2nd ed.; Butterworth-Heinemann: Oxford, UK, 2017; pp. 107–132.

70. Dohda, K.; Yamamoto, M.; Hu, C.; Dubar, L.; Ehmann, K.F. Galling phenomena in metal forming. *Friction* **2021**, *9*, 665–685. [CrossRef]

71. Ostash, O.P.; Kulyk, V.V.; Poznyakov, V.D.; Duriagina, Z.A.; Tepla, T.L. Fatigue crack growth resistance of welded joints simulating the weld-repaired railway wheels metal. *Arch. Mater. Sci. Eng.* **2017**, *86*, 49–55. [CrossRef]
72. Ilie, F.; Covaliu, C. Tribological properties of the lubricant containing titanium dioxide nanoparticles as an additive. *Lubricants* **2016**, *4*, 12. [CrossRef]
73. Cura, M.E.; Trebala, M.; Ge, Y.; Klimczyk, P.; Hannula, S.-P. Mechanical and tribological properties of $WO_{2.9}$ and ZrO_2 + $WO_{2.9}$ composites studied by nanoindentation and reciprocating wear tests. *Wear* **2021**, *478–479*, 203920. [CrossRef]